

Improved Optical Uniformity of WSe₂/WS₂ Moiré Superlattices Grown on hBN toward Quantum Photonics

Yui Tamogami, Wenjin Zhang, Ryotaro Sakakibara, Yuto Urano, Sudhanshu Kumar Nayak, Yusuke Nakanishi, Kenji Watanabe, Takashi Taniguchi, Ryo Kitaura, and Yasumitsu Miyata*



Cite This: *ACS Appl. Nano Mater.* 2026, 9, 8572–8578



Read Online

ACCESS |



Metrics & More



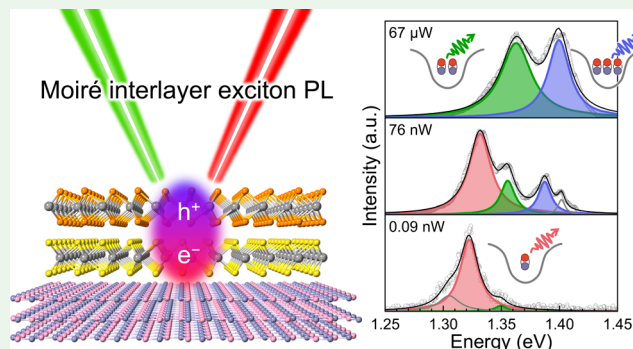
Article Recommendations



Supporting Information

ABSTRACT: Chemical vapor deposition growth offers advantages for producing large-area moiré superlattices with controlled lattice alignment. However, the use of conventional SiO₂/Si substrates often induces inhomogeneous lattice strain that obscures their optical properties. In this work, we report the improved uniformity of WSe₂/WS₂ moiré superlattices directly grown on hexagonal boron nitride (hBN). The hBN-supported samples exhibit well-ordered moiré structures as confirmed by transmission electron microscopy. At low temperatures, they show interlayer exciton peaks that are highly sensitive to excitation power, with a blueshift rate of ~ 120 meV/ μ W, nearly 2 orders of magnitude larger than previously reported. This pronounced shift indicates the enhanced repulsive dipolar interaction of interlayer excitons confined in the moiré potential of WSe₂/WS₂ heterobilayers, enabled by the reduction of inhomogeneous strain and interlayer disorder on hBN. These results highlight the potential of directly grown moiré superlattices on hBN for quantum dot arrays, offering a route toward quantum photonics.

KEYWORDS: 2D materials, transition metal dichalcogenides, moiré superlattices, heterostructures, chemical vapor deposition, interlayer excitons



INTRODUCTION

Transition metal dichalcogenide (TMD)-based moiré superlattices provide a versatile platform for exploring correlated quantum phenomena described by the Hubbard model.^{1–7} For example, carrier-doped moiré systems have exhibited correlated phases such as Mott insulators^{2,3} and generalized Wigner crystals.^{3–6} In addition to carrier doping, a recent study has also reported correlated physics of optically excited electron–hole pairs, namely excitons, in moiré superlattices.⁷ These structures create a nanometer-scale periodic potential that acts as an array of quantum dots hosting optically excited excitons.^{8,9} In particular, certain TMD heterobilayers, such as WS₂/WSe₂, exhibit a type-II band alignment that gives rise to interlayer excitons (IXs) composed of spatially separated electrons and holes.^{10–12} These IXs possess out-of-plane dipoles, leading to repulsive dipole–dipole interactions.^{13–15}

To investigate such excitonic correlations, fabricating high-quality and spatially uniform moiré superlattices is essential. Two main approaches have been employed to fabricate TMD heterobilayers: mechanical transfer of exfoliated monolayers and direct synthesis. The transfer process is relatively simple and widely used, but it often suffers from poor reproducibility and difficulty in scaling up to large areas. In addition, twist-angle deviations between flakes are common, and the process

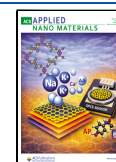
unintentionally introduces bubbles, wrinkles, and contamination, which in turn cause inhomogeneity in the moiré potential.^{16,17} In contrast, chemical vapor deposition (CVD) growth enables scalable fabrication of moiré superlattices with controlled crystallographic alignment and clean interface.^{18–22} However, most growth studies have been performed on SiO₂/Si^{18–21} and sapphire²² substrates, where surface roughness induces lattice strain and spatial nonuniformity in the electronic structure. To suppress such substrate effects, atomically flat substrates such as graphite and hBN provide an attractive platform for growing high-quality monolayers.^{23–25} Recently, TMD-based moiré superlattices have also been synthesized on graphite, and their moiré structure was observed by scanning tunneling microscopy.^{26,27} These developments motivate further optical investigations of such moiré superlattices grown on atomically flat substrates.

Received: January 7, 2026

Revised: April 24, 2026

Accepted: April 24, 2026

Published: May 7, 2026



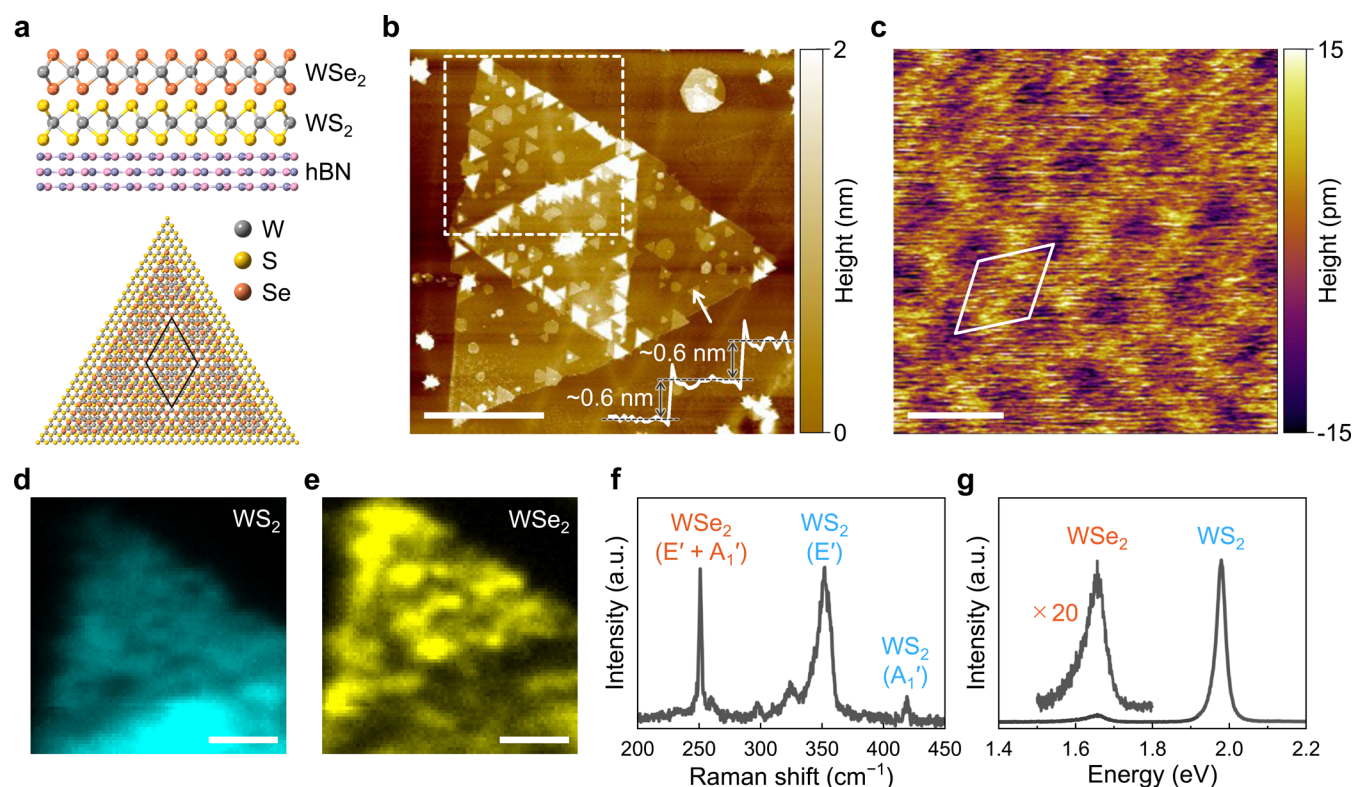


Figure 1. Fabrication and optical characterization of WSe₂/WS₂ heterobilayers. (a) Schematic side and top views of a WSe₂/WS₂ heterobilayer. The lattice mismatch between WSe₂ and WS₂ gives rise to a periodic moiré superlattice in twist-free heterobilayers. The solid line in the top view indicates a moiré unit cell. (b) AFM image of CVD-grown WSe₂/WS₂ heterobilayers on hBN. Scale bar is 5 μm . The inset shows a height profile along the white arrow. (c) Magnified AFM image of the sample. The white solid line outlines a moiré unit cell. A moiré pattern with a period of approximately 8 nm is observed. Scale bar is 10 nm. (d–g) Room-temperature Raman and PL characterization of the WSe₂/WS₂ heterobilayer capped with hBN. Raman intensity maps of (d) the E' mode of WS₂ at 353 cm^{-1} and (e) the E'+A₁' modes of WSe₂ at 251 cm^{-1} , which were obtained from the white box in (b). Scale bars are 2 μm . (f) Raman and (g) PL spectra of the hBN-capped WSe₂/WS₂ heterobilayer.

In this work, we report the characterizations of WSe₂/WS₂ moiré superlattices directly grown on hBN and their low-temperature excitonic properties. The samples grown on hBN exhibit well-ordered moiré structures as confirmed by transmission electron microscopy (TEM). Low-temperature photoluminescence (PL) measurements reveal multiple IX peaks with strong sensitivity to excitation power. The lowest energy peak exhibits a pronounced blueshift rate of $\sim 120 \text{ meV}/\mu\text{W}$, nearly 2 orders of magnitude larger than previously reported. This large shift is attributed to the enhanced repulsive dipolar interaction between IXs trapped in the moiré potential of WSe₂/WS₂ heterobilayers, suggesting the important role of reduced inhomogeneous lattice strain on the hBN substrate. The present system therefore offers a promising route toward quantum dot arrays and related quantum photonic platforms.

EXPERIMENTAL METHODS

WSe₂/WS₂ heterobilayers were grown on exfoliated hBN flakes supported by a SiO₂/Si substrate using a two-step CVD process (Figure S1, see the Supporting Information for experimental details). For the bottom layer, large-area monolayer WS₂ single crystals were prepared by salt-assisted CVD with solid precursors at high temperature. Briefly, monolayer WS₂ was grown on hBN at 970 $^{\circ}\text{C}$ using WO₃ and sulfur as precursors and KBr as a growth promoter.²⁸ The grain size of monolayer WS₂ reached up to 25 μm under these conditions (Figure S2). Monolayer WSe₂ was then grown on the first-grown WS₂ with metal–organic precursors.²⁷ For the WSe₂ growth, the growth temperatures were set to 700–740 $^{\circ}\text{C}$ to avoid the degradation of monolayer WS₂. The temperature dependence of

WSe₂ growth is summarized in Figure S3. For low-temperature optical measurements, the samples were capped with top hBN flake to protect the surface from adsorbates.

RESULTS AND DISCUSSION

Figure 1a shows the structure models of a WSe₂/WS₂ heterobilayer. Because of their lattice mismatch of approximately 4%, twist-free WSe₂/WS₂ heterobilayers are expected to form a moiré superlattice with a wavelength of $\sim 8 \text{ nm}$. Figure 1b shows an atomic force microscopy (AFM) image of the sample grown on hBN. Triangular WSe₂ grains were observed on both monolayer and bilayer WS₂ regions. The height profile indicates that the bottom WS₂ and top WSe₂ layers have a thickness of about 0.6 nm (Figure 1b, inset). Some bright particulate features are also visible in Figure 1b, which originate from locally thicker WSe₂ regions. Both H- and R-type stacking orientations were observed due to the epitaxial growth of WSe₂.¹⁸ In the magnified AFM image of Figure 1c, a moiré pattern with approximately 8 nm was observed, which is consistent with the predicted moiré period for near-zero-twist WSe₂/WS₂ heterobilayers. The formation of WSe₂ was further confirmed by room-temperature Raman and PL analyses performed on samples capped with hBN (Figures 1d–g and S4). The Raman spectrum shows two prominent peaks of the E' mode of WS₂ at 353 cm^{-1} and the E'+A₁' modes of WSe₂ at 251 cm^{-1} (Figure 1f). The absence of Raman peaks in the D- and G-band region indicates that carbon incorporation originating from the organic precursors is negligible (Figure

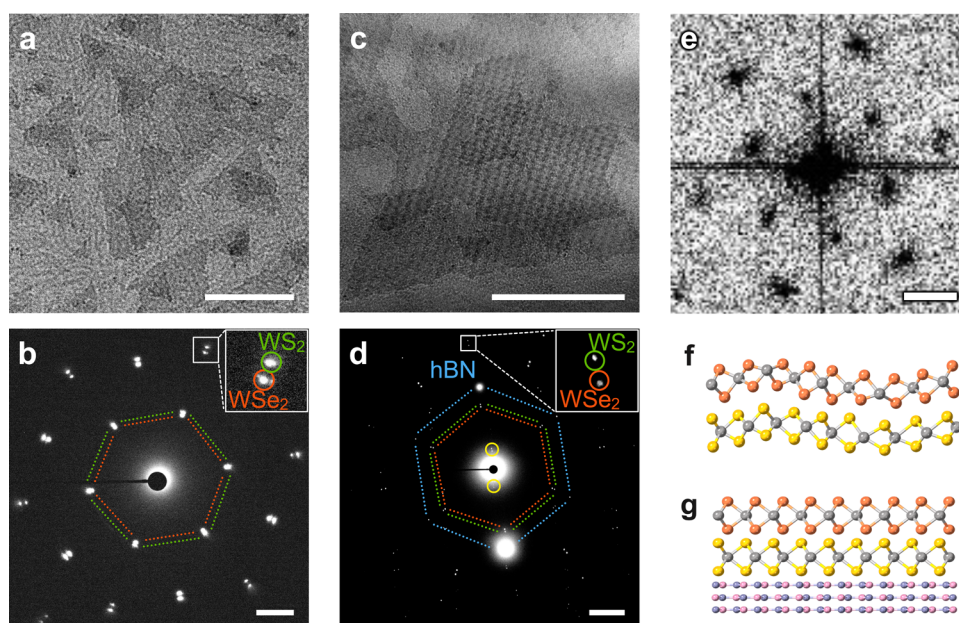


Figure 2. (a) TEM image and (b) SAED pattern of the suspended WSe_2/WS_2 heterobilayer. (c) TEM image, (d) SAED pattern, and (e) FFT pattern (extracted from the central region of Figure S8d) of WSe_2/WS_2 heterobilayer grown on hBN. Schematics of WSe_2/WS_2 heterobilayer showing (f) inhomogeneous lattice strain, and (g) lattice strain suppressed by the hBN substrate. The diffraction spots in (b, d) originating from WS_2 , WSe_2 , and hBN are marked in green, red, and blue, respectively. Scale bars are (a, c) 100 nm, (b, d) 2 nm^{-1} , and (e) 0.1 nm^{-1} .

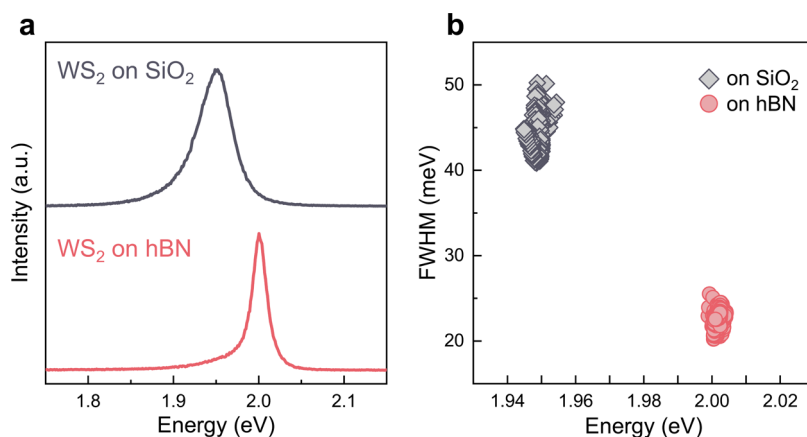


Figure 3. (a) PL spectra and (b) peak positions with FWHM distributions of as-grown (uncapped) monolayer WS_2 on SiO_2 (black) and hBN (red) measured at room temperature.

SS).²⁹ Figure 1d,e present the Raman intensity maps of these modes obtained from the region highlighted by the white box in Figure 1b. The Raman intensity distribution of WSe_2 coincides with the position of the small triangular grains in the AFM image. The PL spectrum also reveals two peaks derived from excitonic emission for WSe_2 at 1.65 eV and WS_2 at 1.98 eV (Figure 1g). The intense PL of WS_2 is mainly due to the monolayer region. In contrast, the emission from WSe_2 is much weaker than that of WS_2 , because of efficient charge transfer in the type II band alignment of the WSe_2/WS_2 heterobilayers. These results clearly demonstrate the formation of WSe_2/WS_2 heterobilayers by a two-step CVD process.

The moiré superlattice of the WSe_2/WS_2 heterobilayer grown on SiO_2 and hBN substrates was then confirmed using TEM, selected-area electron diffraction (SAED), and fast Fourier transform (FFT) analyses. Figure 2a presents a TEM image of a suspended WSe_2/WS_2 film, which was grown on a SiO_2 substrate and subsequently transferred to a TEM grid.

The triangular grains correspond to WSe_2 crystals. Additional scanning transmission electron microscopy (STEM) and TEM images at various magnifications are provided in Figure S6. In a high-magnification image (Figure S6i), a moiré pattern of the WSe_2/WS_2 heterobilayer is observed. Figure 2b shows the SAED pattern of this sample, in which two 6-fold diffraction patterns from WS_2 (green) and WSe_2 (red) are identified.

Figure 2c shows a TEM image of WSe_2/WS_2 heterobilayers grown on hBN. TEM images at different magnifications are provided in Figure S7. Although the grain size of WSe_2 crystals is comparable to that in Figure 2a, a moiré pattern is clearly visible at the same magnification. Figure 2d displays the SAED pattern of this sample, where diffraction spots from hBN (blue), WS_2 (green), and WSe_2 (red) are clearly observed. The alignment of these three patterns confirms van der Waals epitaxy of the stacked layers. While the diffraction spots of WS_2 and WSe_2 in Figure 2b exhibit broadening, this broadening is suppressed when grown on hBN.^{25,30} These observations

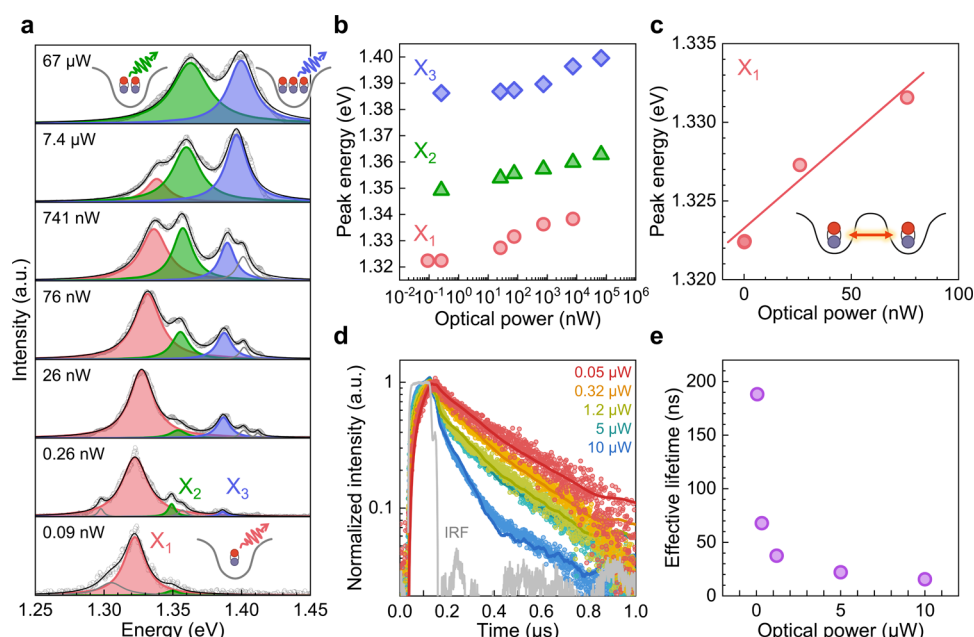


Figure 4. Low-temperature PL and TRPL characteristics of an hBN-encapsulated WSe₂/WS₂ heterobilayer. (a) Optical power dependence (open circles) and Lorentzian fits (solid lines) of the normalized PL spectra at 7.3 K, highlighting three main peaks labeled X₁ (red), X₂ (green), and X₃ (blue). (b) The PL peak energy of X₁, X₂, and X₃ plotted against optical power. (c) The peak energy of X₁ plotted as a function of optical power below 100 nW. The red solid line represents a linear fit. The inset shows a schematic of the long-range repulsive interaction between IXs trapped in neighboring moiré potentials. Error bars are smaller than the data points in (b, c). (d) Normalized TRPL spectra (symbols) measured at 3 K. The solid curves represent biexponential decay fits. The instrument response function (IRF) is shown in gray. (e) Effective lifetimes extracted from the fitted curves in (d), plotted as a function of optical power.

indicate suppression of inhomogeneous lattice strain in the heterobilayer on hBN. We note that it is challenging to quantitatively compare the full width at half-maximum (FWHM) of the diffraction spots because it requires SAED measurements under strictly identical conditions. In addition, two extra diffraction spots are observed around the center of the SAED pattern, as marked with yellow circles in Figure 2d. These spots originate from the moiré periodicities of WS₂/hBN and WSe₂/hBN. The FFT analysis reveals clear superlattice spots from the moiré periodicity of WSe₂/WS₂ around the center (Figures 2e and S8d). From these spots, the moiré wavelength is estimated to be ~ 7.5 nm. In contrast, the FFT of the suspended WSe₂/WS₂ heterobilayer (Figure S8c, inset) shows no superlattice spots, which is attributed to variation in the moiré periodicity. As illustrated in Figure 2f,g, these results highlight that the suppression of inhomogeneous strain by the hBN substrate is crucial for forming uniform moiré superlattices.

To confirm the inhomogeneous strain suppression of samples grown directly on hBN, we measured PL spectra of monolayer WS₂ at room temperature. Figure 3a shows representative PL spectra of monolayer WS₂ grown on SiO₂ (black) and hBN (red). Figure 3b presents the peak positions and corresponding FWHM values measured at various positions within each sample. On average, WS₂ on SiO₂ exhibits a PL peak at 1.95 eV with an FWHM of 43 meV, whereas WS₂ on hBN shows a peak at 2.00 eV and an FWHM of 23 meV, respectively. The blueshift and spectral narrowing are attributed to the relaxation of inhomogeneous tensile strain on hBN.^{23–25} These results also support the importance of hBN as a substrate for achieving uniform heterobilayer growth.

To investigate the effect of the moiré superlattice on the optical response, we measured PL spectra at low temperatures.

All low-temperature optical measurements were performed on an hBN-encapsulated WSe₂/WS₂ heterobilayer (hBN/WSe₂/WS₂/hBN). Figure 4a shows the optical power dependence of the normalized PL spectra of the IXs at 7.3 K, in which multiple distinct peaks are clearly resolved. These peaks were fitted using Lorentzian functions. At the lowest optical power (0.09 nW), a prominent PL peak (X₁) is observed at 1.323 eV. As optical power increases, two additional peaks (X₂ and X₃) appear at higher energy and gradually become dominant. The energy separations between these peaks are measured to be $\Delta E_{21} \sim 27$ meV and $\Delta E_{32} \sim 37$ meV, respectively. The FWHM of the three peaks is typically in the range of 20–30 meV. In addition, all three peaks exhibit a blueshift as optical power increases (Figure 4b). We also measured the temperature dependence of the PL spectra, and the IX features remained observable up to around 100 K (Figure S9). These results are consistent with IXs experiencing moiré-induced confinement and/or interaction-driven energy renormalization as discussed below.

So far, low-temperature PL studies of WS₂/WSe₂ heterobilayers have reported two different spectral behaviors. One is a single PL peak originating from delocalized IXs that predominantly blueshifts with increasing excitation power.³¹ The other is the appearance of multiple IX resonances. For example, Chatterjee *et al.* reported the three IX peaks with near-equal peak spacing at low excitation, whose energies were extracted by multipeak fitting and interpreted as moiré-confined excitonic states.³² Multiple IX resonances can be also described by a bosonic Hubbard model, in which multiple IXs occupying the same moiré site interact via onsite dipole–dipole repulsion.¹⁵ Within this model, the energy of an *n*-exciton state in the same moiré site is given by

$$E_n = nE_X + \frac{U}{2}n(n-1)$$

where E_X is the energy of X_1 , and U represents the exciton Hubbard interaction strength associated with the onsite dipolar repulsion. Previous studies report a theoretically calculated U of approximately 34 meV and an experimentally determined range of 30–37 meV.^{15,33} In our experiment, the energy separations ($\Delta E_{21} \sim 27$ meV and $\Delta E_{32} \sim 37$ meV) are qualitatively consistent with these previous studies. Moreover, the relation $\Delta E_{21} < \Delta E_{32}$ reflects enhanced onsite repulsion due to the exciton phase-space filling effect, as reported previously.¹⁵ We therefore attribute the three peaks (X_1 – X_3) to the presence of one, two, and three IXs per moiré site. Notably, resolving such discrete resonances requires narrow emission line widths, implying a spatially uniform moiré potential within the excitation spot. In previous studies, the IX line width is highly sample-dependent. This variability strongly affects whether multiple resonances can be spectrally resolved, thereby contributing to divergent interpretations of the IX peak structure. This suggests that our samples provide a useful platform for investigating interaction-driven moiré exciton physics.

While the multiple-peak structure can be understood in terms of onsite repulsion within a single moiré site, we now focus on the power-dependent continuous blueshifts that reflect repulsive interactions between IXs in different moiré sites. As shown in Figure 4b, all three peaks systematically blueshift with increasing optical power. In the low-power regime, X_1 exhibits a particularly strong power dependence, showing a blueshift rate of ~ 120 meV/ μ W based on a linear fit below 100 nW (Figure 4c). This blueshift can be interpreted as arising from long-range repulsive interactions between IXs trapped in neighboring moiré sites (Figure 4c, inset).^{15,32–34} In this picture, the energy shift δE is known to be proportional to the effective IX density n ($\delta E \propto n$).^{32,34} This relationship is qualitatively consistent with the present results. Notably, the observed blueshift rate is 2 orders of magnitude larger than values reported previously.^{15,32–34} For comparison, the highest blueshift rate reported in the literature is approximately 1 meV/ μ W.³² This unusually large blueshift suggests strong exciton–exciton interactions, which may reflect a spatially uniform moiré potential and/or extended IX lifetimes in our samples.

At higher excitation powers, the blueshift gradually saturates (Figure S10). This behavior is attributed to density-dependent nonradiative processes, such as excitonic Auger recombination³¹ and exciton–exciton annihilation,³⁵ which suppress the increase in the IX population with excitation power. Such behavior can also be observed in the exciton dynamics, as discussed below.

To gain further insight into the exciton dynamics, we performed time-resolved PL (TRPL) measurements of IXs at 3 K under various optical powers (Figure 4d). Figure 4e presents the effective lifetimes extracted from biexponential fits as a function of optical power. At the lowest power (0.05 μ W), the fit yields an effective lifetime of about 180 ns. This lifetime is notably longer than those reported in previous studies on similar WSe₂/WS₂ moiré superlattices.^{31–34,36} As the excitation power increases, the effective lifetime decreases. This behavior is consistent with enhanced density-dependent nonradiative processes, as discussed above.^{31,35} The combination of a pronounced power-dependent blueshift and a long lifetime at

low excitation suggests strong localization and limited diffusion of IXs in the moiré potential. These observations are consistent with improved uniformity of the moiré superlattice in our directly grown samples on hBN, which can minimize inhomogeneous strain fluctuations and interfacial disorder.

Finally, we note the optical uniformity of the present samples and the remaining challenges. The moiré superlattices grown on hBN exhibit enhanced uniformity compared to those grown on SiO₂. This improvement is evidenced by reduced spectral line widths in room-temperature PL measurements, as well as by sharp electron diffraction spots observed. However, the PL peak position and spectral shape still vary across different regions (Figure S11), indicating the influence of residual lattice strain and/or impurities on the moiré potential. Possible contributing factors include the transfer process of the top hBN layer and the use of mechanically exfoliated hBN. Moreover, triangular WSe₂ grains exhibit both H- and R-type stacking orientations as shown in Figure 1b. Since the heterobilayer domain size (~ 1 μ m) is comparable to the laser spot diameter, the measured PL may originate from H-type, R-type, or a mixture of both stacking configurations, which could further contribute to the observed spatial variation. Addressing these issues remains an important direction for future studies.

CONCLUSIONS

We have directly grown WSe₂/WS₂ moiré superlattices on hBN substrates, which effectively suppress the interlayer impurities and substrate-induced inhomogeneous lattice strain. The improved sample uniformity enabled us to observe blueshift rates of IXs on the order of hundreds of meV/ μ W, as well as long exciton lifetimes. We also observed multiple-IX occupation of moiré sites and estimated the onsite repulsive dipole–dipole interaction energies. These results demonstrate that combining the CVD process with an atomically flat hBN surface provides a useful route to uniform TMD-based moiré superlattices, offering a pathway toward quantum photonics.

ASSOCIATED CONTENT

Supporting Information

The Supporting Information is available free of charge at <https://pubs.acs.org/doi/10.1021/acsanm.6c00104>.

Experimental details; schematic illustration of the salt-assisted CVD and metal-organic CVD systems; optical and PL images of WS₂ grown on hBN by CVD; AFM images of WSe₂/WS₂ synthesized on hBN at different temperatures; PL intensity maps of WSe₂/WS₂ grown on hBN; extended Raman spectrum of an as-grown WSe₂/WS₂ heterobilayer; STEM and TEM images of suspended WSe₂/WS₂ heterobilayers; TEM images of WSe₂/WS₂ heterobilayers grown on hBN; TEM images and FFT patterns of suspended and hBN-supported WSe₂/WS₂ moiré superlattices; temperature-dependent PL spectra of the IX emission; PL peak energy of X_1 , X_2 , and X_3 plotted against optical power on a linear scale; and position dependence of PL spectra at low temperatures (PDF)

■ AUTHOR INFORMATION

Corresponding Author

Yasumitsu Miyata — Research Center for Materials Nanoarchitectonics (MANA), National Institute for Materials Science (NIMS), Tsukuba 305-0044, Japan; Department of Physics, Tokyo Metropolitan University, Hachioji 192-0397, Japan; Email: miyata.yasumitsu@nims.go.jp

Authors

Yui Tamogami — Research Center for Materials Nanoarchitectonics (MANA), National Institute for Materials Science (NIMS), Tsukuba 305-0044, Japan; Department of Physics, Tokyo Metropolitan University, Hachioji 192-0397, Japan

Wenjin Zhang — Research Center for Materials Nanoarchitectonics (MANA), National Institute for Materials Science (NIMS), Tsukuba 305-0044, Japan; Department of Physics, Tokyo Metropolitan University, Hachioji 192-0397, Japan

Ryotaro Sakakibara — Research Center for Materials Nanoarchitectonics (MANA), National Institute for Materials Science (NIMS), Tsukuba 305-0044, Japan; Department of Physics, Tokyo Metropolitan University, Hachioji 192-0397, Japan

Yuto Urano — Research Center for Materials Nanoarchitectonics (MANA), National Institute for Materials Science (NIMS), Tsukuba 305-0044, Japan; Graduate School of Chemical Sciences and Engineering, Hokkaido University, Hokkaido 060-8628, Japan

Sudhanshu Kumar Nayak — Research Center for Materials Nanoarchitectonics (MANA), National Institute for Materials Science (NIMS), Tsukuba 305-0044, Japan; Department of Physics, Indian Institute of Technology Hyderabad, Telangana 502285, India

Yusuke Nakanishi — Department of Advanced Materials Science, The University of Tokyo, Kashiwa 277-8561, Japan

Kenji Watanabe — Research Center for Electronic and Optical Materials, National Institute for Materials Science (NIMS), Tsukuba 305-0044, Japan

Takashi Taniguchi — Research Center for Materials Nanoarchitectonics (MANA), National Institute for Materials Science (NIMS), Tsukuba 305-0044, Japan

Ryo Kitaura — Research Center for Materials Nanoarchitectonics (MANA), National Institute for Materials Science (NIMS), Tsukuba 305-0044, Japan; Graduate School of Chemical Sciences and Engineering, Hokkaido University, Hokkaido 060-8628, Japan

Complete contact information is available at:

<https://pubs.acs.org/10.1021/acsnm.6c00104>

Author Contributions

Y.M. developed the concept and supervised the project. Y.T. and Y.M. prepared and characterized the materials. Y.T. and R.S. carried out the TEM and STEM observations. Y.T., R.K., Y.M., W.Z., Y.U., and S.K.N. performed low-temperature and time-resolved PL measurements. T.T. and K.W. provided the high-quality hBN. Y.T., W.Z., R.S., and Y.M. prepared the figures and wrote the manuscript with feedback from the other authors. All authors have approved the final version of the manuscript.

Notes

The authors declare no competing financial interest.

■ ACKNOWLEDGMENTS

This work was supported by the Japan Science and Technology Agency (JST), the JST FOREST Program (JPMJFR213X) and the JST CREST (JPMJCR23A4, JPMJCR24A5), and Kakenhi Grants-in-Aid (JP21H05232, JP21H05234, JP22H04957, JP22H00280, JP24H00044, and JP23H02052) from the Japan Society for the Promotion of Science (JSPS). MANA is supported by World Premier International Research Center Initiative (WPI), MEXT, Japan. We acknowledge H. Sugawara for conducting the AFM measurements.

■ REFERENCES

- (1) Tang, Y.; Li, L.; Li, T.; Xu, Y.; Liu, S.; Barmak, K.; Watanabe, K.; Taniguchi, T.; MacDonald, A. H.; Shan, J.; Mak, K. F. Simulation of Hubbard Model Physics in WSe_2/WS_2 Moiré Superlattices. *Nature* **2020**, *579* (7799), 353–358.
- (2) Lian, Z.; Meng, Y.; Ma, L.; Maity, I.; Yan, L.; Wu, Q.; Huang, X.; Chen, D.; Chen, X.; Chen, X.; Blei, M.; Taniguchi, T.; Watanabe, K.; Tongay, S.; Lischner, J.; Cui, Y.-T.; Shi, S.-F. Valley-Polarized Excitonic Mott Insulator in WS_2/WSe_2 Moiré Superlattice. *Nat. Phys.* **2024**, *20*, 34–39.
- (3) Regan, E. C.; Wang, D.; Jin, C.; Utama, M. I. B.; Gao, B.; Wei, X.; Zhao, S.; Zhao, W.; Zhang, Z.; Yumigeta, K.; Blei, M.; Carlström, J. D.; Watanabe, K.; Taniguchi, T.; Tongay, S.; Crommie, M.; Zettl, A.; Wang, F. Mott and Generalized Wigner Crystal States in WSe_2/WS_2 Moiré Superlattices. *Nature* **2020**, *579* (7799), 359–363.
- (4) Huang, X.; Wang, T.; Miao, S.; Wang, C.; Li, Z.; Lian, Z.; Taniguchi, T.; Watanabe, K.; Okamoto, S.; Xiao, D.; Shi, S.; Cui, Y.-T. Correlated Insulating States at Fractional Fillings of the WS_2/WSe_2 Moiré Lattice. *Nat. Phys.* **2021**, *17*, 715–719.
- (5) Li, H.; Li, S.; Regan, E. C.; Wang, D.; Zhao, W.; Kahn, S.; Yumigeta, K.; Blei, M.; Taniguchi, T.; Watanabe, K.; Tongay, S.; Zettl, A.; Crommie, M. F.; Wang, F. Imaging Two-Dimensional Generalized Wigner Crystals. *Nature* **2021**, *597* (7878), 650–654.
- (6) Zhou, Y.; Sung, J.; Brutschea, E.; Esterlis, I.; Wang, Y.; Scuri, G.; Gelly, R. J.; Heo, H.; Taniguchi, T.; Watanabe, K.; Záránd, G.; Lukin, M. D.; Kim, P.; Demler, E.; Park, H. Bilayer Wigner Crystals in a Transition Metal Dichalcogenide Heterostructure. *Nature* **2021**, *595* (7865), 48–52.
- (7) Xiong, R.; Nie, J. H.; Brantly, S. L.; Hays, P.; Sailus, R.; Watanabe, K.; Taniguchi, T.; Tongay, S.; Jin, C. Correlated Insulator of Excitons in WSe_2/WS_2 Moiré Superlattices. *Science* **2023**, *380* (6647), 860–864.
- (8) Tran, K.; Moody, G.; Wu, F.; Lu, X.; Choi, J.; Kim, K.; Rai, A.; Sanchez, D. A.; Quan, J.; Singh, A.; Embley, J.; Zepeda, A.; Campbell, M.; Autry, T.; Taniguchi, T.; Watanabe, K.; Lu, N.; Banerjee, S. K.; Silverman, K. L.; Kim, S.; Tutuc, E.; Yang, L.; MacDonald, A. H.; Li, X. Evidence for Moiré Excitons in van der Waals Heterostructures. *Nature* **2019**, *567* (7746), 71–75.
- (9) Yu, H.; Liu, G.-B.; Tang, J.; Xu, X.; Yao, W. Moiré Excitons: From Programmable Quantum Emitter Arrays to Spin-Orbit-Coupled Artificial Lattices. *Sci. Adv.* **2017**, *3* (11), No. e1701696.
- (10) Lin, B.-H.; Chao, Y.-C.; Hsieh, I. T.; Chuu, C.-P.; Lee, C.-J.; Chu, F.-H.; Lu, L.-S.; Hsu, W.-T.; Pao, C.-W.; Shih, C.-K.; Su, J.-J.; Chang, W.-H. Remarkably Deep Moiré Potential for Intralayer Excitons in $\text{MoSe}_2/\text{MoS}_2$ Twisted Heterobilayers. *Nano Lett.* **2023**, *23* (4), 1306–1312.
- (11) Shinokita, K.; Miyauchi, Y.; Watanabe, K.; Taniguchi, T.; Matsuda, K. Resonant Coupling of a Moiré Exciton to a Phonon in a $\text{WSe}_2/\text{MoSe}_2$ Heterobilayer. *Nano Lett.* **2021**, *21* (14), S938–S944.
- (12) Rivera, P.; Schaibley, J. R.; Jones, A. M.; Ross, J. S.; Wu, S.; Aivazian, G.; Klement, P.; Seyler, K.; Clark, G.; Ghimire, N. J.; Yan, J.; Mandrus, D. G.; Yao, W.; Xu, X. Observation of Long-Lived

Interlayer Excitons in Monolayer MoSe₂-WSe₂ Heterostructures. *Nat. Commun.* **2015**, *6* (1), No. 6242.

(13) Li, W.; Lu, X.; Dubey, S.; Devenica, L.; Srivastava, A. Dipolar Interactions between Localized Interlayer Excitons in van der Waals Heterostructures. *Nat. Mater.* **2020**, *19* (6), 624–629.

(14) Kremser, M.; Brotons-Gisbert, M.; Knörzer, J.; Gückelhorn, J.; Meyer, M.; Barbone, M.; Stier, A. V.; Gerardot, B. D.; Müller, K.; Finley, J. J. Discrete Interactions between a Few Interlayer Excitons Trapped at a MoSe₂-WSe₂ Heterointerface. *npj 2D Mater. Appl.* **2020**, *4* (1), No. 8.

(15) Park, H.; Zhu, J.; Wang, X.; Wang, Y.; Holtzmann, W.; Taniguchi, T.; Watanabe, K.; Yan, J.; Fu, L.; Cao, T.; Xiao, D.; Gamelin, D. R.; Yu, H.; Yao, W.; Xu, X. Dipole Ladders with Large Hubbard Interaction in a Moiré Exciton Lattice. *Nat. Phys.* **2023**, *19* (9), 1286–1292.

(16) Seyler, K. L.; Rivera, P.; Yu, H.; Wilson, N. P.; Ray, E. L.; Mandrus, D. G.; Yan, J.; Yao, W.; Xu, X. Signatures of Moiré-Trapped Valley Excitons in MoSe₂/WSe₂ Heterobilayers. *Nature* **2019**, *567* (7746), 66–70.

(17) Naito, H.; Makino, Y.; Zhang, W.; Ogawa, T.; Endo, T.; Sannomiya, T.; Kaneda, M.; Hashimoto, K.; Lim, H. E.; Nakanishi, Y.; Watanabe, K.; Taniguchi, T.; Matsuda, K.; Miyata, Y. High-Throughput Dry Transfer and Excitonic Properties of Twisted Bilayers Based on CVD-Grown Transition Metal Dichalcogenides. *Nanoscale Adv.* **2023**, *5* (18), S115–S121.

(18) Yuan, L.; Zheng, B.; Kunstmann, J.; Brumme, T.; Kuc, A. B.; Ma, C.; Deng, S.; Blach, D.; Pan, A.; Huang, L. Twist-Angle-Dependent Interlayer Exciton Diffusion in WS₂-WSe₂ Heterobilayers. *Nat. Mater.* **2020**, *19* (6), 617–623.

(19) Wu, X.; Wang, X.; Li, H.; Zeng, Z.; Zheng, B.; Zhang, D.; Li, F.; Zhu, X.; Jiang, Y.; Pan, A. Vapor Growth of WSe₂/WS₂ Heterostructures with Stacking Dependent Optical Properties. *Nano Res.* **2019**, *12* (12), 3123–3128.

(20) Zhang, W.; Liu, Z.; Nakajo, H.; Aoki, S.; Wang, H.; Wang, Y.; Gao, Y.; Maruyama, M.; Kawakami, T.; Makino, Y.; Kaneda, M.; Chen, T.; Aso, K.; Ogawa, T.; Endo, T.; Nakanishi, Y.; Watanabe, K.; Taniguchi, T.; Oshima, Y.; Yamada-Takamura, Y.; Koshino, M.; Okada, S.; Matsuda, K.; Kato, T.; Miyata, Y. Chemically Tailored Semiconductor Moiré Superlattices of Janus Heterobilayers. *Small Struct.* **2024**, *5* (5), No. 2470022.

(21) Xu, M.; Ji, H.; Zheng, L.; Li, W.; Wang, J.; Wang, H.; Luo, L.; Lu, Q.; Gan, X.; Liu, Z.; Wang, X.; Huang, W. Reconfiguring Nucleation for CVD Growth of Twisted Bilayer MoS₂ with a Wide Range of Twist Angles. *Nat. Commun.* **2024**, *15* (1), No. 562.

(22) Choi, J.; Hsu, W.-T.; Lu, L.-S.; Sun, L.; Cheng, H.-Y.; Lee, M.-H.; Quan, J.; Tran, K.; Wang, C.-Y.; Staab, M.; Jones, K.; Taniguchi, T.; Watanabe, K.; Chu, M.-W.; Gwo, S.; Kim, S.; Shih, C.-K.; Li, X.; Chang, W.-H. Moiré Potential Impedes Interlayer Exciton Diffusion in van der Waals Heterostructures. *Sci. Adv.* **2020**, *6* (39), No. eaba8866.

(23) Kobayashi, Y.; Sasaki, S.; Mori, S.; Hibino, H.; Liu, Z.; Watanabe, K.; Taniguchi, T.; Suenaga, K.; Maniwa, Y.; Miyata, Y. Growth and Optical Properties of High-Quality Monolayer WS₂ on Graphite. *ACS Nano* **2015**, *9* (4), 4056–4063.

(24) Okada, M.; Sawazaki, T.; Watanabe, K.; Taniguchi, T.; Hibino, H.; Shinohara, H.; Kitaura, R. Direct Chemical Vapor Deposition Growth of WS₂ Atomic Layers on Hexagonal Boron Nitride. *ACS Nano* **2014**, *8* (8), 8273–8277.

(25) Zhang, X.; Zhang, F.; Wang, Y.; Schulman, D. S.; Zhang, T.; Bansal, A.; Alem, N.; Das, S.; Crespi, V. H.; Terrones, M.; Redwing, J. M. Defect-Controlled Nucleation and Orientation of WSe₂ on hBN: A Route to Single-Crystal Epitaxial Monolayers. *ACS Nano* **2019**, *13* (3), 3341–3352.

(26) Zhang, C.; Chu, C.-P.; Ren, X.; Li, M.-Y.; Li, L.-J.; Jin, C.; Chou, M.-Y.; Shih, C.-K. Interlayer Couplings, Moiré Patterns, and 2D Electronic Superlattices in MoS₂/WSe₂ Hetero-Bilayers. *Sci. Adv.* **2017**, *3* (1), No. e1601459.

(27) Kobayashi, Y.; Yoshida, S.; Maruyama, M.; Mogi, H.; Murase, K.; Maniwa, Y.; Takeuchi, O.; Okada, S.; Shigekawa, H.; Miyata, Y.

Continuous Heteroepitaxy of Two-Dimensional Heterostructures Based on Layered Chalcogenides. *ACS Nano* **2019**, *13* (7), 7527–7535.

(28) Wada, N.; Pu, J.; Takaguchi, Y.; Zhang, W.; Liu, Z.; Endo, T.; Irisawa, T.; Matsuda, K.; Miyauchi, Y.; Takenobu, T.; Miyata, Y. Efficient and Chiral Electroluminescence from In-Plane Heterostructure of Transition Metal Dichalcogenide Monolayers. *Adv. Funct. Mater.* **2022**, *32* (40), No. 2203602.

(29) Choudhury, T. H.; Simchi, H.; Boichot, R.; Chubarov, M.; Mohney, S. E.; Redwing, J. M. Chalcogen Precursor Effect on Cold-Wall Gas-Source Chemical Vapor Deposition Growth of WS₂. *Cryst. Growth Des.* **2018**, *18* (8), 4357–4364.

(30) Man, M. K. L.; Deckoff-Jones, S.; Winchester, A.; Shi, G.; Gupta, G.; Mohite, A.; Kar, S.; Kioupakis, E.; Talapatra, S.; Dani, K. Protecting the Properties of Monolayer MoS₂ on Silicon Based Substrates with an Atomically Thin Buffer. *Sci. Rep.* **2016**, *6*, No. 20890.

(31) Cai, C.-S.; Lai, W.-Y.; Liu, P.-H.; Chou, T.-C.; Liu, R.-Y.; Lin, C.-M.; Gwo, S.; Hsu, W.-T. Ultralow Auger-Assisted Interlayer Exciton Annihilation in WS₂/WSe₂ Moiré Heterobilayers. *Nano Lett.* **2024**, *24* (9), 2773–2781.

(32) Chatterjee, S.; Dandu, M.; Dasika, P.; Biswas, R.; Das, S.; Watanabe, K.; Taniguchi, T.; Raghunathan, V.; Majumdar, K. Harmonic to Anharmonic Tuning of Moiré Potential Leading to Unconventional Stark Effect and Giant Dipolar Repulsion in WS₂/WSe₂ Heterobilayer. *Nat. Commun.* **2023**, *14* (1), No. 4679.

(33) Kai, F.; Wang, X.; Xie, Y.; Yang, Y.; Watanabe, K.; Taniguchi, T.; Yu, H.; Yao, W.; Cui, X. Distinct Moiré Exciton Dynamics in WS₂/WSe₂ Heterostructure. *Quantum Front.* **2025**, *4* (1), No. 2.

(34) Sun, X.; Zhu, Y.; Qin, H.; Liu, B.; Tang, Y.; Lü, T.; Rahman, S.; Yildirim, T.; Lu, Y. Enhanced Interactions of Interlayer Excitons in Free-Standing Heterobilayers. *Nature* **2022**, *610* (7932), 478–484.

(35) Yuan, L.; Huang, L. Exciton Dynamics and Annihilation in WS₂ 2D Semiconductors. *Nanoscale* **2015**, *7* (16), 7402–7408.

(36) Miao, S.; Wang, T.; Huang, X.; Chen, D.; Lian, Z.; Wang, C.; Blei, M.; Taniguchi, T.; Watanabe, K.; Tongay, S.; Wang, Z.; Xiao, D.; Cui, Y.-T.; Shi, S.-F. Strong Interaction between Interlayer Excitons and Correlated Electrons in WSe₂/WS₂ Moiré Superlattice. *Nat. Commun.* **2021**, *12* (1), No. 3608.